Structural basis for substrate discrimination and integrin binding by autotaxin

Jens Hausmann[1,7], **Satwik Kamtekar**[2,7], **Evangelos Christodoulou**[1], **Jacqueline E. Day**[2], **Tao Wu**[3], **Zachary Fulkerson**[3], **Harald M.H.G. Albers**[4], **Laurens A. van Meeteren**[4], **Anna Houben**[4], **Leonie van Zeijl**[4], **Silvia Jansen**[5], **Maria Andries**[5], **Troii Hall**[2], **Lyle E. Pegg**[2], **Timothy E. Benson**[2], **Mobien Kasiem**[1], **Karl Harlos**[6], **Craig Vander Kooi**[3], **Susan S. Smyth**[3], **Huib Ovaa**[4], **Mathieu Bollen**[5], **Andrew J. Morris**[3], **Wouter H. Moolenaar**[4], and **Anastassis Perrakis**[1]

[1]Division of Biochemistry, The Netherlands Cancer Institute, Plesmanlaan 121, 1066 CX Amsterdam, The Netherlands [2]Pfizer Global Research and Development, Chesterfield, MO 63017, USA [3]Division of Cardiovascular Medicine, University of Kentucky, Lexington, KY 40536, USA [4]Division of Cell Biology, The Netherlands Cancer Institute, Plesmanlaan 121, 1066 CX Amsterdam, The Netherlands [5]Laboratory of Biosignaling & Therapeutics, Department of Molecular Cell Biology, University of Leuven, B-3000 Leuven, Belgium [6]Division of Structural Biology, Wellcome Trust Centre for Human Genetics, University of Oxford, Oxford, UK

Abstract

Autotaxin (ATX) or ecto-nucleotide pyrophosphatase/phosphodiesterase-2 (ENPP2) is a secreted lysophospholipase D that generates the lipid mediator lysophosphatidic acid (LPA), a mitogen and chemo-attractant for many cell types. ATX-LPA signaling has roles in various pathologies including tumour progression and inflammation. However, the molecular basis of substrate recognition and catalysis, and the mechanism of interaction with target cells, has been elusive.

Here we present the crystal structure of ATX, alone and in complex with a small-molecule inhibitor. We identify a hydrophobic lipid-binding pocket and map key residues required for catalysis and selection between nucleotide and phospholipid substrates. We show that ATX interacts with cell-surface integrins via its N-terminal somatomedin-B-like domains, using an atypical mechanism. Our results define determinants of substrate discrimination by the ENPP family, suggest how ATX promotes localized LPA signaling, and enable new approaches to target ATX with small-molecule therapeutics.

Autotaxin (ATX), also known as ecto-nucleotide pyrophosphatase/phosphodiesterase 2 (ENPP2), is a secreted glycoprotein[1] that acts as a lysophospholipase D (lysoPLD), converting lysophosphatidylcholine (LPC) into the lipid mediator lysophosphatidic acid (LPA)[2,3]. LPA acts on specific G protein-coupled receptors eliciting responses ranging from chemotaxis and neurite remodelling to cell proliferation and survival[4,5]. The ATX-LPA signalling axis is implicated in vascular and neural development[6–9], tumour progression and metastasis[10–15], as well as inflammation[16], fibrotic disease[17,18] and neuropathic pain[19]. As such, ATX holds promise as an attractive and easily accessible therapeutic target. We and others have recently described potent small-molecule inhibitors of ATX that are capable of lowering LPA levels in the circulation[20,21].

ATX is a ~100 kDa glycoprotein that has several distinct domains (Fig. 1a). At the N-terminus it harbours two consecutive cysteine-rich somatomedin-B-like (SMB) domains, a fold known to be involved in protein-protein interactions[22]. The ATX SMB domains are attractive candidates for mediating the demonstrated binding of ATX to activated platelets and lymphocytes in an integrin-dependent manner[16,23], thereby providing a possible route for localized LPA production and signalling at sites of injury and inflammation. The central catalytic phosphodiesterase (PDE) domain follows the SMB domains. It is similar to the catalytic domain of alkaline phosphatases, and its closest homologue with a known structure is a well-characterised bacterial phosphodiesterase[24]. Finally, at its C-terminus, ATX contains a nuclease-like (NUC) domain, which is catalytically inert and has been suggested to be involved in substrate binding and presentation[25].

ATX/ENPP2 is one of seven mammalian ENPP type ectophosphodiesterases[26], containing central PDE domains. Due to lack of structural data, the molecular basis for the diverse substrate preferences of ENPP family enzymes is not well understood. For example, the phosphodiesterase activity of the founding member ENPP1, a protein that has been implicated in the aetiology of mineralisation diseases and diabetes, is nucleotide-selective, whereas ATX/ENPP2 preferentially hydrolyzes lysophospholipids although it also accepts nucleotides as substrates.

The most potent small-molecule inhibitor we have recently described[21] contains a boronic acid, designed to specifically bind to the catalytic threonine of ATX. A structure-based mechanistic understanding of how boron binds to the threonyl nucleophile, and of the details of substrate recognition and catalysis by ATX will accelerate the further development of selective ATX inhibitors.

To understand how the domains of ATX are organized, their role in determining selectivity for lipid over nucleotide substrates, how our boronic acid inhibitors interact with ATX, and how the integrin-mediated interaction with platelets takes place, we determined the crystal structure of ATX/ENPP2; in this paper we present the structure of ATX from rat (*r*ATX) and the structure-based biochemical analysis of human ATX (*h*ATX).

Results

The crystal structure of Autotaxin

We determined the crystal structure of the full-length secreted form of rat ATX (*r*ATX), which is 93% identical to the human enzyme *h*ATX (Supplementary Fig.1). A variant of *r*ATX, in which two of the three glycosylation sites were mutated, leaving the single site needed for activity[27], was produced in HEK293 cells, purified and crystallised[28,29]. The structure was determined to 2.0Å resolution by a combination of molecular replacement and single-wavelength anomalous dispersion (Table 1).

*r*ATX presents a compact and robust architecture for a multi-domain protein (Fig. 1); two differently packed crystal forms show virtually identical domain placement (Fig. 1b,c). The two N-terminal cysteine-rich somatomedin-B-like (SMB) domains and the C-terminal nuclease-like (NUC) domain contact opposing sides of the catalytic phosphodiesterase (PDE) domain.

The structures of the individual domains of *r*ATX (Fig. 1a) all resemble known folds (Fig. 2). The N-terminal SMB domains are structurally similar to both the SMB domain of vitronectin[22] and that of ENPP1 (PDB:2YS0, unpublished) (Fig. 2a). The catalytic PDE domain is most similar to the *Xanthomonas axonopodis* nucleotide pyrophosphatase[24] (*Xa*NPP) (Fig. 2b). The catalytic residues of ATX and *Xa*NPP, including the catalytic Thr209 and Thr90 respectively, are also well conserved (Fig. 3a). The closest structural match to the C-terminal NUC domain is the cyanobacterial nuclease NucA[30] (Fig. 2c), but none of the catalytic residues in NucA is conserved in the ATX NUC domain, accounting for its previously observed catalytic inactivity.

The PDE-NUC domain interface

The PDE and NUC domains are tethered together in a strikingly rigid manner. The interface area is 1280 Å^2, reinforced by seven hydrogen bonds and nine salt bridges. Many elements of the PDE domain participate in this interaction, while only the C-terminal region (802–859) of the NUC domain is involved. The two domains are tethered by an intermolecular Cys-bridge between residues 413 and 805 (Fig. 1d) that is essential for retaining catalytic activity[25]. Moreover, a large `lasso' loop of 50 residues (540–589), starting at the end of the PDE domain, wraps tightly around the NUC domain (Fig. 1c), finally entering the fold from the side opposite to the PDE domain. Furthermore, the first two N-acetyl-glucosamine moieties of the essential Asn-524-linked glycan chain[27] are packed between the PDE and NUC domains (Fig. 1e), forming an interface area of 321 Å^2. Finally, the C-terminal region from residues 829–850, which is essential for secretion[25], as well as Lys852, which is required for catalytic activity[25], are also in the domain interface (Fig. 1f). In the structure,

Lys852 makes two salt bridges with Glu830 and Asp836 and is presumably important for positioning the C-terminal helix. It thus appears that evolution has selected for an extended range of interactions that bind the catalytically dead NUC domain to the active PDE domain.

The NUC domain of ATX (and ENPP1 and ENPP3) encompasses an EF-hand-like (EFL) motif26 ([739]DYNYDGLRDTEDE[751]), crucial for activity for ENPP1 and ENPP331, but reportedly not for ENPP232. This 13-residue EFL motif binds Ca^{+2} (Supplementary Fig. 2a), but is not flanked by helices. Notably, its first residue, Asp739, bridges to Lys430 and is the only residue outside the C-terminus of the NUC domain that interacts with the PDE domain (Supplementary Fig. 2b). ATX mutated at this site (K430A) was as active as the wild-type enzyme, but a significant amount was retained intracellularly (Supplementary Fig. 2d). Furthermore, the secreted fraction of ATX (K430A) was more sensitive to thermal denaturation than wild-type ATX (Supplementary Fig. 2e), suggesting that the salt bridge between Lys430 and Asp739 contributes to stabilization of the PDE-NUC interface. Mutation of three residues of the EFL motif (D739S/N741A/D743S) abolished secretion of ATX (Supplementary Fig.2d). The mutant proteins that accumulated intracellularly showed strongly reduced activity (Supplementary Fig.2e), consistent with previous findings for ENPP1 and ENPP331.

The phosphodiesterase catalytic site

The PDE domains of ATX and *Xa*NPP24 share similar architectures with fully conserved catalytic residues (Fig. 3a,b). At the active site, the Zn^{+2} atom proximal to the catalytic Thr209 (Thr210 in *h*ATX) is coordinated by the side chains of two aspartates and one histidine (Asp171, Asp358, His359), whereas the distal zinc is coordinated by one aspartate and two histidines (Asp311, His315, His474).

An asparagine residue (Asn230; Asn 231 in *h*ATX) faces the two metal ions in a position similar to that of Asn111 in *Xa*NPP. Asn111 was shown in *Xa*NPP not only to be important for catalysis but also to confer specificity for phosphodiester bond hydrolysis24; an arginine substitution at this position favoured phosphatase activity. In *h*ATX, the N231A mutation significantly impairs the catalytic activity against both phospholipid and nucleotide substrates (Fig. 4a,b). Since ATX hydrolyzes ATP to generate AMP and pyrophosphate rather than ADP and phosphate, Asn230 is likely responsible for this preference for diester against monoester hydrolysis.

In one of the ATX crystal forms we located a phosphate ion (Fig. 3a, Supplementary Fig. 3a) that matches the positions occupied in *Xa*NPP complex structures by the α-phosphate of AMP, or the transition state analogue vanadate (Fig. 2b). These similarities suggest a conserved catalytic mechanism, in which the activated Oγ nucleophile of Thr209 attacks the phosphate group of a substrate, resulting in the formation of a transition state involving a phosphate ester linkage24. The intermediate can then be hydrolyzed to the products, i.e. LPA or AMP.

The substrate and inhibitor binding pocket

ATX hydrolyzes both nucleotide and phospholipid substrates, at least *in vitro*. The location of the nucleotide binding site in ATX can be inferred from the structure of *Xa*NPP bound to AMP (Fig. 3f). The shape of this site remains fully conserved in ATX (Fig. 3e). These two enzymes, and other ENPP family members, are therefore expected to bind nucleotides in a similar manner.

ATX-mediated LPC hydrolysis is specifically and potently inhibited by a series of small-molecule boronic acid inhibitors that lower plasma LPA levels in mice following intravenous administration[21]. We determined a structure of *r*ATX in complex with one of these inhibitors, HA15533 (Fig. 3c; Supplementary Fig.3b,c, Table 1), which enables us to correlate the activity of this inhibitor with its binding mode and make inferences about lipid substrate binding. The boron atom on one end of the inhibitor forms a reversible covalent bond with the nucleophile hydroxyl group of Thr209. One of the two boron hydroxyl groups is further stabilized between the two zinc ions. A search of the protein data bank did not yield any other structures in which a borate moiety is similarly complexed by two zinc ions and a threonyl nucleophile[34]. The rest of the hydrophobic four-ring system of HA155 forms an extended network of van der Waals contacts, with an interaction interface of 574 Å^2. The first two aromatic rings of HA155 assume positions similar to those of the ribose and the adenine in the structure of *Xa*NPP bound to AMP (Fig. 3c,e). The third, thiazolidinedione, ring would not be accommodated by the *Xa*NPP structure (Fig. 3d). The last aromatic ring, a hydrophobic fluoro-benzene, is pointing directly into a deep hydrophobic pocket, oriented perpendicular to the protein surface.

We hypothesize that this hydrophobic pocket also binds the acyl chain of lysophospholipid substrates. We used High Ambiguity Driven DOCKing (HADDOCK[35]) to create a model of the binding of LPC(14:0) to our structure of *r*ATX. Fig. 3g,h shows how the acyl chain can be easily accommodated in this pocket. The model also demonstrates that the pocket is large enough to accommodate only a single aliphatic chain, and explains how ATX sterically excludes di-acyl phospholipids. It is noteworthy that our model is consistent with previously reported biochemical data: for example, the change of Leu213 (Leu214 in *h*ATX), one of the hydrophobic residues lining the pocket and contacting the modeled substrate, to a polar histidine has been shown to decrease LPC hydrolysis[36].

To validate our model further, we constructed additional binding site mutants and examined their activity. These mutagenesis studies employed *h*ATX (residue numbers in the human enzyme are n+1 compared to the rat enzyme above, owing to a single residue insertion after residue 37). *h*ATX and catalytically inactive *h*ATX T210A were used as controls to evaluate activity of the hydrophobic binding pocket mutants: F211A, Y307Q, L214H, F275Q, A305E, F274E, A218V, S170E (Fig. 4a). All mutants were expressed at levels similar to the wild-type enzyme. They were quantified and assayed in an LPC hydrolysis assay using saturating concentrations of LPC(14:0), the optimal substrate *in vitro* (Fig. 3c). All of these hydrophobic pocket mutants showed reduced lysoPLD activity levels when compared to wild-type *h*ATX (Fig. 4b).

The A218V mutant, which has about half the activity of *h*ATX, targets a residue deep in the hydrophobic pocket and alters LPC selectivity (Fig. 4a). This mutant hydrolyzes short-chain LPCs more efficiently than the wild-type protein (Fig. 4c). This can be explained by the presence of a bulkier valine residue at the bottom of the pocket, which possibly mediates a better contact with *e.g.* LPC(12:0), but excludes substrates with longer acyl chains. A218V and similar mutations that alter the acyl chain length selectivity could provide useful tools for probing the biological role and significance of ATX in generating distinct molecular species of LPA.

Many of the binding cleft variants differentially affect LPC and nucleotide hydrolysis. Although all of them are less active in the LPC hydrolysis assay, some can still hydrolyze nucleotide substrates with near wild-type activity. These include the previously reported L214H mutant and the novel mutants S170E, A218V and A305E (Fig. 4b), which target the acyl chain lipid binding region of the pocket. In contrast, the Y307Q or F211Y mutants, which target the region of the binding site that accommodates both nucleotides and lipids, are significantly less active against both lipid and nucleotide substrates. In fact, these two variants are comparatively less active against nucleotides than lipids, possibly because these mutations have a greater effect on the bulkier nucleoside moiety than the glycerol group of the lipid substrates. These observations suggest that the hydrophobic binding pocket is an extension of the nucleotide binding site that specifically accommodate lysophospholipid acyl chains, without affecting nucleotide binding.

When the structures of ATX and *Xa*NPP are superimposed, a stretch of 18 amino acids in *Xa*NPP occupies the space corresponding to the hydrophobic binding pocket of ATX. This stretch of amino acids in *Xa*NPP thus precludes it from accommodating lysophospholipids (Fig. 2b). Sequence alignments indicate that while ATX has a deletion in this region, *Xa*NPP and ENPP1 do not (Supplementary Fig. 1). The presence of this stretch of amino acids in ENPP1 and *Xa*NPP therefore explains why they cannot hydrolyze lysophospholipids, and why ENPP1 is insensitive to ATX inhibitors such as HA155[21].

The SMB domains and interaction with integrins

The two N-terminal Cys-rich SMB domains in ATX (atxSMB1 and atxSMB2) provide the first structural instances of these domains in the context of an intact protein. The structure of the SMB domain of the plasma protein vitronectin (vSMB) is known, both alone and in complex with the plasminogen activator inhibitor-1[37] (PAI-1, Fig. 5a) and the urokinase-type plasminogen activator[38] (uPAR) (Fig. 5b). The structural organization of the SMB domain cysteine knot fold, comprising four pairs of crossed disulfide bonds, had been the subject of considerable debate[22,39]. The organization of the atxSMB domains is consistent with the vitronectin SMB X-ray and NMR structures, as well as with the NMR structure of the ENPP1 SMB domain (PDB:2YS0, unpublished).

Both atxSMB domains form extensive interactions with the catalytic PDE domain (Fig. 5c,d). The interaction between the atxSMB1 domain and the PDE domain involves approximately the same surface that mediates the vSMB to PAI-1 and uPAR interactions. However, atxSMB2 uses an unusual interface for interaction with the PDE domain, leaving the surface more typically used for protein-protein interactions available to engage with

other binding partners (Fig. 5d). We examined whether hATX can interact with PAI-1 by co-expression and immuno-precipitation experiments, but detected no interaction (Supplementary Fig. 4).

ATX binds to activated platelets in a β3 integrin-dependent manner and mediates static adhesion of platelets to immobilized ATX23. By analogy with the well characterised vSMB-mediated interactions with integrins, we considered the possibility that the ATX SMB domains also interact with platelet integrins. We found that a truncated protein containing only the two ATX SMB domains (53–143, atxSMB) strongly binds to activated human platelets (Fig. 5f,g). Binding to the SMB domains is enhanced by stimulating the platelets with ADP or the integrin activator Mn^{+2} and is substantially attenuated by the β3 integrin blocking antibody 7E3 (Fig. 5f). Moreover, binding of the isolated SMB domains to platelets is comparable to that of full-length ATX, in both avidity and concentration dependence (Supplementary Fig. 5a). From these results we conclude that the N-terminal SMB domains are the primary mediators of the ATX-platelet interaction with β3 integrins on the agonist-stimulated platelet surface.

The atxSMB2 domain contains an integrin-binding sequence RGD motif (126–128, Fig. 5d,e). However, this motif lies within the atxSMB2 domain, whereas the vitronectin RGD motif is located several residues downstream from its SMB domain and is disordered37. In vitronectin, an RGD to RGE mutation disrupts an Asp-mediated Mn^{2+} interaction between the ligand and integrin thereby severely attenuating integrin binding. An ATX RGE mutant, however, shows binding to activated platelets indistinguishable from that of wild-type ATX (Supplemental Fig. 5b). Binding of platelets to the isolated SMB domains containing an AGA mutant (R127A/D129A) showed less binding compared to the wild-type SMB domain protein (Fig. 5g and Supplemental Fig. 6), but did not abolish it as expected. This suggested that the interaction of ATX with platelet β3 integrins is mechanistically distinct from the binding of the vitronectin SMB domain to these receptors, and involves residues separate from the RGD motif. To examine this notion further, we created five additional mutants of the atxSMB2 domain: E110A, R112A, H119A, D121A and E122A. Of these, only H119A and E122A were expressed in amounts sufficient for purification and further experiments. While E122A abrogated binding to an extent similar to that of the AGA mutant, the H119A mutation showed significantly reduced binding. Glu122 is conserved in the vSMB, while His119 is a Gln (maintaining the nitrogen donor at a similar position), and both these residues participate in the interaction of vSMB with PAI-1 and uPAR. These experiments confirm that binding of ATX to integrins involves a wider portion of the available atxSMB2 surface, which includes His119, Asp122 as well as Asp129.

The SMB domains are involved in LPA binding

AtxSMB2 abuts the lipid-binding pocket and a nearby narrow tunnel (the `white hole' in Fig. 3h). In both crystal forms residual electron density occupies this tunnel (Supplemental Fig. 7), likely indicating the presence of a molecule that we were unable to model, possibly a lipid acquired from the growth medium. The proximity of the SMB domains to the lipid-binding site and the tunnel raises the possibility that they might be involved in product binding and release.

To test if the SMB domains modulate the enzymatic activity of ATX, we expressed an ATX variant lacking both SMB1 and SMB2 (SMB-ATX; residues 145–863 of *h*ATX). We have previously reported that LPA acts as a mixed-type inhibitor of ATX activity against a variety of substrates40. We could thus probe the role played by the SMB domains in product binding and release by comparing LPA-mediated inhibition of nucleotide hydrolysis in wild-type ATX and SMB-ATX. Both wild-type ATX and the SMB-ATX protein exhibited comparable activity against the classical nucleotide substrate pNP-TMP, with k_M values of 1.93±0.20 and 2.87±0.9 mM respectively (Supplemental Fig. 8). However, whereas wild-type ATX activity against this substrate was potently inhibited by LPA(18:1) (EC_{50} 0.08 μM), SMB-ATX was approximately 10-fold less sensitive (EC_{50} 0.72 μM) to inhibition by this LPA species (Fig. 4d). These results identify a role for the SMB domains as a determinant of the affinity of the interaction between ATX and LPA, and are consistent with our suggestion that SMB2 participates in substrate recognition and/or product release. Processes that impact on the interaction between SMB2 and the PDE domain, for example integrin binding, could constitute a mechanism for physiological regulation of ATX activity.

Discussion

We have determined the crystal structure of rat ATX and tested the activities of structurally guided site- directed mutants in human ATX. Since the enzymes from the two species are 93% identical, the biochemical and structural experiments readily complement one another.

A deep, hydrophobic pocket of the type observed in ATX is a thermodynamically unstable structure. We suggest that the formation of strong interactions between the NUC and PDE domains during the course of evolution, may have stabilized the fold sufficiently for it to accommodate the deletion of eighteen residues (Supplemental Fig. 1) and the consequent formation of the hydrophobic pocket.

The determinants of the substrate specificity of the ENPPs have long been a mystery. The ATX structure provides a possible explanation. Both nucleotides and lipids partially share the same binding pocket, but the acyl-chain of lipid substrates form additional hydrophobic contacts with ATX. This model implies that the LPA product likely has higher affinity for ATX than any nucleotide substrate. This hypothesis is consistent with our previous finding that LPA acts as an inhibitor of ATX activity against a variety of substrates40, but not of LPC hydrolysis33. Thus, LPA formed by the enzyme may act as a "substrate specifying factor" that effectively inhibits the hydrolysis of nucleotides because it can only be displaced by lysophospholipid substrates such as LPC. This mechanism could dictate ATX activity *in vivo*, because the spectrum of available LPA species could define ATX activity against specific lysophospholipid substrates. Our findings also suggest that further analysis of structural determinants of substrate discrimination could lead to the identification of molecules that inhibit the hydrolysis of specific substrates, *e.g.* long-chain rather than short-chain LPC species.

The ATX SMB domains function as protein interaction modules, mediating platelet interaction through integrin binding. However, the binding mode appears to be structurally distinct from classical RGD-mediated integrin binding. Instead, ATX-SMB2 may interact

with integrins using a surface similar to that employed by the related vitronectin SMB domains in their interactions with PAI-1 and uPAR.

We also have shown that the SMB domains are important for binding the LPA product to ATX, and we speculate that they might be involved in LPA release. In this scenario, SMB-mediated interactions with integrins might not only provide a mechanism for recruiting ATX to the cell surface to generate LPA in proximity of its receptors, but could also mediate a conformational change to promote product release. Localized LPA production by integrin-mediated recruitment of ATX (*e.g.* at the platelet surface) may account for the observed increase in plasma LPA levels following platelet activation[41]. Similar reasoning may also be applied to ENPP1, where a natural mutation of lysine 173 (K173Q, often described in literature as `K121Q'), that is equivalent to the Arg128 of the ATX RGD motif, has severe physiological consequences[42] suggesting that modulation of integrin binding to the SMB domains through such mutations may result in altered ENPP1/2 activities *in vivo*.

Further structural and biochemical studies examining ATX with its physiological substrates, products and specific integrin subunits, will be necessary to unravel how exactly LPA production is regulated by ATX.

Methods

Protein production, crystallization and diffraction data collection

All protocols are described in references 28,29. The HA155 inhibitor was mixed in three-molar excess with *r*ATX and co-crystallized in conditions similar to the native data form[28].

Structure solution and refinement

Crystallographic statistics are shown in Table 1. Structure solution was performed using PHASER[43] in the hybrid molecular replacement - single anomalous dispersion mode. We used the structure of *Xa*NPP (2GSN[24]) as a search model, with non-conserved side chains truncated to the last common atom between residues. A clear rotation function solution was obtained (Z-score 15.01), sufficient to orient the single molecule of the asymmetric unit in the P1 space group. Using the phase probability distribution from that solution, PHASER identified ten heavy atom sites, using the anomalous differences from the zinc and iodine ions, resulting in phases with a figure of merit of 0.4. Solvent flattening followed by automated model building with ARP/wARP[44] resulted in 737 residues distributed in 8 chains. The model was completed manually using COOT[45], interspersed with reciprocal space refinement cycles in REFMAC5[46]. The final model was validated using the MolProbity[47] server, and is of excellent quality without any Ramachandran outliers, ranking in the 93rd best percentile of PDB structures in that resolution. The second native crystal form, without Iodine in the crystallization conditions, was solved by molecular replacement and refined; apart from minor differences in disordered regions the two models are identical. The HA155 complex was determined by molecular replacement using the native ATX model without ions; the difference map showed clear density for the omitted zinc ions and the HA155 ligand. This structure was refined with autoBUSTER[48]. After adjusting protein regions, HA155 was modeled and refined using a dictionary generated by PRODRG[49] and

manually adjusted to conform to the tetrahedral geometry expected for the reversibly covalent bound boron atom. Validation with Molprobity shows 96.2% of all residues in Ramachandran favored regions, ranking in the 100th percentile for that resolution.

Structure analysis

Structural similarity searches were performed with SSM50 using default parameters. All interface calculations were performed with PISA51. The reported interface area is the difference in the accessible surface of isolated and interacting structures divided by two.

The HADDOCK web server was used35 for docking a flexible LPC molecule into the structure of *r*ATX. The phosphate atom was restrained to a position consistent with the observed phosphate in the AMP:*Xa*NPP complex. The binding pocket residues that were in contact with the HA155 inhibitor were treated as `active' residues that make contacts with the LPC substrate. All other parameters were used with default values. Docking experiment resulted to a single cluster of 200 structures.

Site directed mutagenesis

All constructs were made using standard molecular biology procedures and verified by sequencing.

Protein production for EF-hand mutants

Cells were transiently transfected at 30–40% confluency using Fugene. The medium was collected 72 h later and the cells were lysed in 50 mM Tris/HCl, pH 7.5, 150 mM NaCl, 1% (w/v) Triton X-100 supplemented with 0.5 mM PMSF and 0.5 mM benzamide. After three freeze-thaw-cycles and ultracentrifugation (30 min at 100,000g) the supernatant was collected and used as `cell lysate' in Western blots and to determine NPP2 activity.

Protein production for binding site mutants

HEK293 cells were transiently transfected at 30–40% confluency using Fugene-6. The medium was collected 96 h later and used for pNP-TMP assays and LPC assays. Protein levels were quantified by Western blot.

ATX/lysoPLD activity assay

ATX lysoPLD activity was measured by the release of choline from LPC21. Briefly, medium from transfected HEK293 cells containing approximately 5 nM *h*ATX (quantified by Western blot analysis using purified wild-type ATX as a standard), was incubated with 500 μM LPC species in Tris-HCl buffer (pH 7.4), 0.01% (w/v) Triton X-100 for 4 h at 37 C. Liberated choline was detected colorimetrically using choline oxidase (1 Unit mL^{-1}), horseradish peroxidase (2 Unit mL^{-1}) and homovanillic acid (HVA) (2 mM). Fluorescence was determined at $\lambda_{ex}/\lambda_{em}$=320/450nm in 96-well plates.

Nucleotide phosphodiesterase assay

ATX nucleotide phosphodiesterase activity was measured colorimetrically using the nucleotide derivative pNP-TMP (p-nitrophenyl thymidine 5′-monophosphate) as a

substrate40. 15 nM *h*ATX of the preparations used also for the lysoPLD assay above, was incubated with 1 mM pNP-TMP in glycine-buffered saline at pH 9.5 in 96-well plates. The amount of liberated para-nitrophenolate (pNP) was determined by the absorbance at 405 nm for 3 h. For investigations of LPA inhibition, incubations contained 0.01% (w/v) Triton X-100 and varying concentrations of LPA(18:1).

Protein production for platelet binding assays and LPA inhibition experiments

ATX proteins were generated by expression in CHO cells using variants of pSecTag engineered to fuse an IgK leader sequence and furin protease site N-terminal of a His6 sequence. Secreted proteins were purified from conditioned medium and concentrated to ~1 mg ml^{-1} for use in binding assays.

Static platelet adhesion assays

The interaction of ATX to activated platelets was studied by measuring binding of calcein labeled platelets to fibrinogen, ATX or fragments using a microtiter plate assay as described previously23. In brief, human platelets were isolated from citrate anticoagulated blood. Platelets were labeled by incubation with 7 mM calcein-AM and 150 nM PGI2 and then isolated by gel filtration using Sepharose 2B eluted with Tyrodes buffer (12 mM NaHCO$_3$, 138 mM NaCl, 5.5 mM glucose, 2.9 mM KCl, 10 mM HEPES, 0.35% (w/v) fatty-acid-free BSA, pH 7.35). ATX, ATX fragments or fibrinogen were diluted in 50 mM Tris pH 7.4 100 mM NaCl and incubated in a Microfluor 96-well plate for 16 h at 4° C. The wells were washed and blocked by incubation with Tyrodes buffer for 1 h at RT. Gel filtered platelets were diluted 200 times in Tyrodes buffer containing 2 mM CaCl$_2$, 1 mM MgCl$_2$ and platelet activators, small molecule inhibitors or blocking antibodies. After incubation for 60 min at RT, wells were washed with Tyrodes buffer containing 2 mM CaCl$_2$, 1 mM MgCl$_2$ and bound platelets were quantified by measurement of calcein fluorescence.

Supplementary Material

Refer to Web version on PubMed Central for supplementary material.

Acknowledgments

References

1. Stracke ML, et al. Identification, purification, and partial sequence analysis of autotaxin, a novel motility-stimulating protein. J Biol Chem. 1992; 267:2524–2529. [PubMed: 1733949]

2. Tokumura A, et al. Identification of human plasma lysophospholipase D, a lysophosphatidic acid-producing enzyme, as autotaxin, a multifunctional phosphodiesterase. J Biol Chem. 2002; 277:39436–39442. [PubMed: 12176993]

3. Umezu-Goto M, et al. Autotaxin has lysophospholipase D activity leading to tumor cell growth and motility by lysophosphatidic acid production. J Cell Biol. 2002; 158:227–233. [PubMed: 12119361]

4. Noguchi K, Herr D, Mutoh T, Chun J. Lysophosphatidic acid (LPA) and its receptors. Curr Opin Pharmacol. 2009; 9:15–23. [PubMed: 19119080]

5. van Meeteren LA, Moolenaar WH. Regulation and biological activities of the autotaxin-LPA axis. Prog Lipid Res. 2007; 46:145–160. [PubMed: 17459484]

6. van Meeteren LA, et al. Autotaxin, a secreted lysophospholipase D, is essential for blood vessel formation during development. Mol Cell Biol. 2006; 26:5015–5022. [PubMed: 16782887]

7. Tanaka M, et al. Autotaxin stabilizes blood vessels and is required for embryonic vasculature by producing lysophosphatidic acid. J Biol Chem. 2006; 281:25822–25830. [PubMed: 16829511]

8. Koike S, et al. Autotaxin/lysophospholipase D-mediated lysophosphatidic acid signaling is required to form distinctive large lysosomes in the visceral endoderm cells of the mouse yolk sac. J Biol Chem. 2009; 284:33561–33570. [PubMed: 19808661]

9. Fotopoulou S, et al. ATX expression and LPA signalling are vital for the development of the nervous system. Dev Biol. 339:451–464. [PubMed: 20079728]

10. Lin S, et al. The absence of LPA2 attenuates tumor formation in an experimental model of colitis-associated cancer. Gastroenterology. 2009; 136:1711–1720. [PubMed: 19328876]

11. Liu S, et al. Expression of autotaxin and lysophosphatidic acid receptors increases mammary tumorigenesis, invasion, and metastases. Cancer Cell. 2009; 15:539–550. [PubMed: 19477432]

12. Mills GB, Moolenaar WH. The emerging role of lysophosphatidic acid in cancer. Nat Rev Cancer. 2003; 3:582–591. [PubMed: 12894246]

13. Nam SW, et al. Autotaxin (ATX), a potent tumor motogen, augments invasive and metastatic potential of ras-transformed cells. Oncogene. 2000; 19:241–247. [PubMed: 10645002]

14. Taghavi P, et al. In vitro genetic screen identifies a cooperative role for LPA signaling and c-Myc in cell transformation. Oncogene. 2008; 27:6806–6816. [PubMed: 18762810]

15. David M, et al. Cancer cell expression of autotaxin controls bone metastasis formation in mouse through lysophosphatidic acid-dependent activation of osteoclasts. PLoS One. 5:e9741. [PubMed: 20305819]

16. Kanda H, et al. Autotaxin, an ectoenzyme that produces lysophosphatidic acid, promotes the entry of lymphocytes into secondary lymphoid organs. Nat Immunol. 2008; 9:415–423. [PubMed: 18327261]

17. Pradere JP, et al. LPA1 receptor activation promotes renal interstitial fibrosis. J Am Soc Nephrol. 2007; 18:3110–3118. [PubMed: 18003779]

18. Tager AM, et al. The lysophosphatidic acid receptor LPA1 links pulmonary fibrosis to lung injury by mediating fibroblast recruitment and vascular leak. Nat Med. 2008; 14:45–54. [PubMed: 18066075]

19. Inoue M, et al. Initiation of neuropathic pain requires lysophosphatidic acid receptor signaling. Nat Med. 2004; 10:712–718. [PubMed: 15195086]

20. Gierse JK, et al. A Novel Autotaxin Inhibitor Reduces Lysophosphatidic Acid Levels in Plasma and the Site of Inflammation. J Pharmacol Exp Ther.

21. Albers HM, et al. Boronic acid-based inhibitor of autotaxin reveals rapid turnover of LPA in the circulation. Proc Natl Acad Sci U S A.

22. Zhou A. Functional structure of the somatomedin B domain of vitronectin. Protein Sci. 2007; 16:1502–1508. [PubMed: 17567740]

23. Pamuklar Z, et al. Autotaxin/lysopholipase D and lysophosphatidic acid regulate murine hemostasis and thrombosis. J Biol Chem. 2009; 284:7385–7394. [PubMed: 19139100]

24. Zalatan JG, Fenn TD, Brunger AT, Herschlag D. Structural and functional comparisons of nucleotide pyrophosphatase/phosphodiesterase and alkaline phosphatase: implications for mechanism and evolution. Biochemistry. 2006; 45:9788–9803. [PubMed: 16893180]

25. Jansen S, Andries M, Derua R, Waelkens E, Bollen M. Domain interplay mediated by an essential disulfide linkage is critical for the activity and secretion of the metastasis-promoting enzyme autotaxin. J Biol Chem. 2009; 284:14296–14302. [PubMed: 19329427]

26. Stefan C, Jansen S, Bollen M. NPP-type ectophosphodiesterases: unity in diversity. Trends Biochem Sci. 2005; 30:542–550. [PubMed: 16125936]

27. Jansen S, et al. An essential oligomannosidic glycan chain in the catalytic domain of autotaxin, a secreted lysophospholipase-D. J Biol Chem. 2007; 282:11084–11091. [PubMed: 17307740]

28. Day JE, et al. Crystallization and preliminary X-ray diffraction analysis of rat autotaxin. Acta Crystallographica Section F. 2010; 66:1127–1129.

29. Hausmann J, et al. Mammalian cell expression, purification, crystallization and microcrystal data collection of autotaxin/ENPP2, a secreted mammalian glycoprotein. Acta Crystallographica Section F. 2010; 66:1130–1135.

30. Ghosh M, Meiss G, Pingoud A, London RE, Pedersen LC. Structural insights into the mechanism of nuclease A, a betabeta alpha metal nuclease from Anabaena. J Biol Chem. 2005; 280:27990–27997. [PubMed: 15897201]

31. Bollen M, Gijsbers R, Ceulemans H, Stalmans W, Stefan C. Nucleotide pyrophosphatases/phosphodiesterases on the move. Crit Rev Biochem Mol Biol. 2000; 35:393–432. [PubMed: 11202013]

32. Lee J, et al. Enzymatic activation of autotaxin by divalent cations without EF-hand loop region involvement. Biochem Pharmacol. 2001; 62:219–224. [PubMed: 11389881]

33. Albers HM, et al. Boronic acid-based inhibitor of autotaxin reveals rapid turnover of LPA in the circulation. Proc Natl Acad Sci U S A. 2010; 107:7257–7262. [PubMed: 20360563]

34. Golovin A, Henrick K. MSDmotif: exploring protein sites and motifs. BMC Bioinformatics. 2008; 9:312. [PubMed: 18637174]

35. de Vries SJ, van Dijk M, Bonvin AM. The HADDOCK web server for data-driven biomolecular docking. Nat Protoc. 2010; 5:883–897. [PubMed: 20431534]

36. Cimpean A, Stefan C, Gijsbers R, Stalmans W, Bollen M. Substrate-specifying determinants of the nucleotide pyrophosphatases/phosphodiesterases NPP1 and NPP2. Biochem J. 2004; 381:71–77. [PubMed: 15096095]

37. Zhou A, Huntington JA, Pannu NS, Carrell RW, Read RJ. How vitronectin binds PAI-1 to modulate fibrinolysis and cell migration. Nat Struct Biol. 2003; 10:541–544. [PubMed: 12808446]

38. Huai Q, et al. Crystal structures of two human vitronectin, urokinase and urokinase receptor complexes. Nat Struct Mol Biol. 2008; 15:422–423. [PubMed: 18376415]

39. Li X, Zou G, Yuan W, Lu W. Defining the native disulfide topology in the somatomedin B domain of human vitronectin. J Biol Chem. 2007; 282:5318–5326. [PubMed: 17189256]

40. van Meeteren LA, et al. Inhibition of autotaxin by lysophosphatidic acid and sphingosine 1-phosphate. J Biol Chem. 2005; 280:21155–21161. [PubMed: 15769751]

41. Eichholtz T, Jalink K, Fahrenfort I, Moolenaar WH. The bioactive phospholipid lysophosphatidic acid is released from activated platelets. Biochem J. 1993; 291(Pt 3):677–680. [PubMed: 8489494]

42. Prudente S, Morini E, Trischitta V. Insulin signaling regulating genes: effect on T2DM and cardiovascular risk. Nat Rev Endocrinol. 2009; 5:682–693. [PubMed: 19924153]

43. McCoy AJ. Solving structures of protein complexes by molecular replacement with Phaser. Acta Crystallogr D Biol Crystallogr. 2007; 63:32–41. [PubMed: 17164524]

44. Langer G, Cohen SX, Lamzin VS, Perrakis A. Automated macromolecular model building for X-ray crystallography using ARP/wARP version 7. Nat Protoc. 2008; 3:1171–1179. [PubMed: 18600222]

45. Emsley P, Cowtan K. Coot: model-building tools for molecular graphics. Acta Crystallogr D Biol Crystallogr. 2004; 60:2126–2132. [PubMed: 15572765]

46. Murshudov GN, Vagin AA, Dodson EJ. Refinement of macromolecular structures by the maximum-likelihood method. Acta Crystallogr D Biol Crystallogr. 1997; 53:240–255. [PubMed: 15299926]

47. Davis IW, et al. MolProbity: all-atom contacts and structure validation for proteins and nucleic acids. Nucleic Acids Res. 2007; 35:W375–383. [PubMed: 17452350]

48. Blanc E, et al. Refinement of severely incomplete structures with maximum likelihood in BUSTER-TNT. Acta Crystallogr D Biol Crystallogr. 2004; 60:2210–2221. [PubMed: 15572774]

49. Schuttelkopf AW, van Aalten DM. PRODRG: a tool for high-throughput crystallography of protein-ligand complexes. Acta Crystallogr D Biol Crystallogr. 2004; 60:1355–1363. [PubMed: 15272157]

50. Krissinel E, Henrick K. Secondary-structure matching (SSM), a new tool for fast protein structure alignment in three dimensions. Acta Crystallogr D Biol Crystallogr. 2004; 60:2256–2268. [PubMed: 15572779]

51. Krissinel E, Henrick K. Inference of macromolecular assemblies from crystalline state. J Mol Biol. 2007; 372:774–797. [PubMed: 17681537]
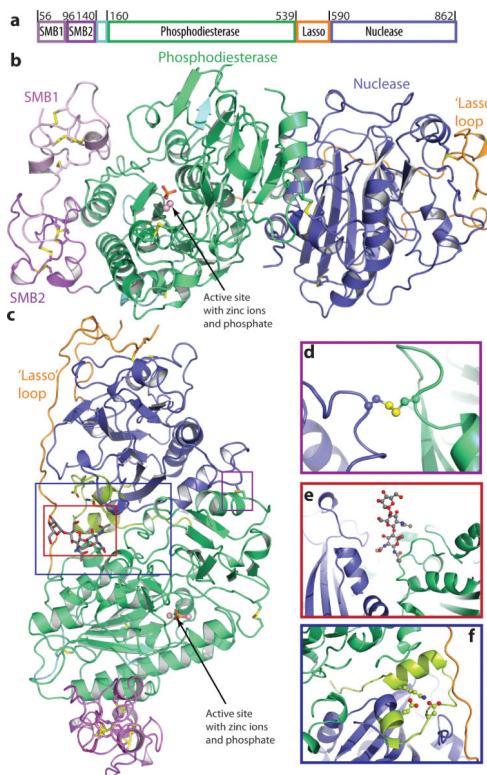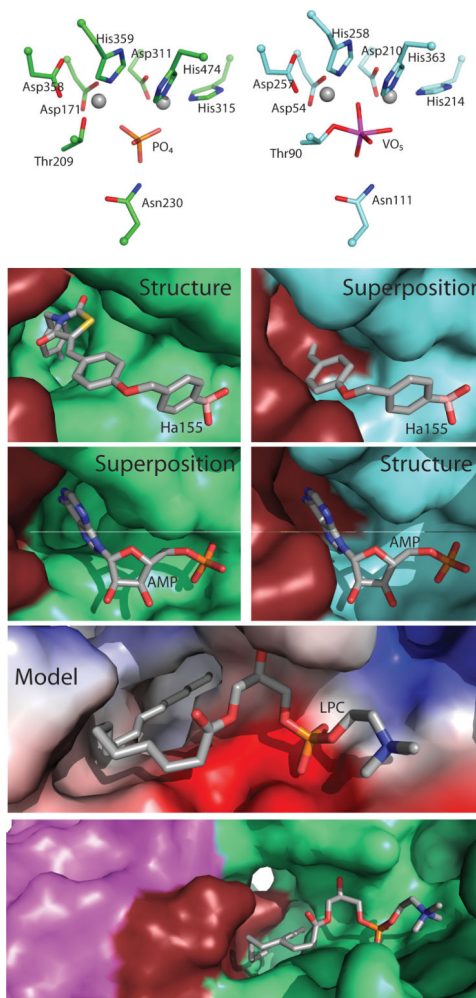
Figure 1.

The structure of ATX. (**a**) A schematic view of the domain structure of ATX; (**b**) Cartoon representation with the SMB domains coloured in pink and magenta, the PDE domain in green, the NUC domain in blue, the lasso loop wrapping around the NUC domain in orange (the lasso loop interacts with the rest of the proteins through 18 hydrogen bonds, 8 salt bridges, and a disulphide bond between residues 566 and 666) and the short loop connecting the SMB domains to the PDE domain in cyan; the phosphate and the zinc ions bound to the active site as well as cystine bridges are shown in stick-and-sphere representation, with the S_γ atoms in yellow, phosphorous in orange, zinc in pink; (**c**) The same cartoon as above in a different orientation, showing the active site with the bound phosphate and zinc ions and the lasso loop wrapping around the NUC domain to the left; the colored boxes relate to panels (d,e,f) showing the interface between the PDE and NUC domains; (**d**) The essential Cys-bridge that connects the PDE and NUC domains. (**e**) The essential glycan chain; (**f**) the C-terminal helix highlighted in lemon-green, with the important Lys-852 and its two salt-bridge partners, Glu-830 and Asp-836. All structural figures were created with Pymol (http://www.pymol.org)
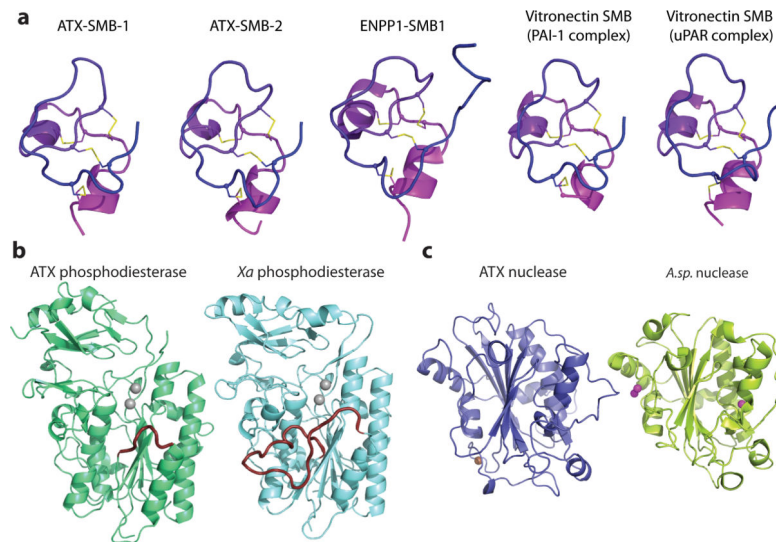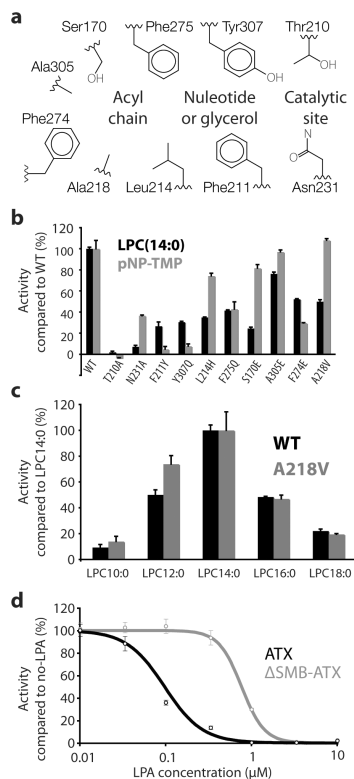
Figure 2.

ATX domains and closest structural homologues. (**a**) The two SMB domains of ATX/ENPP2, the ENPP SMB1 domain (PDB:2YS0, unpublished), and two structures of the vitronectin SMB domain (PDB:1OC037, 3BT138) are shown side by side, colored blue to magenta from N to C terminus with cystine bridges shown as sticks, with the S_γ atom atoms in yellow. The ATX SMB domains share 38% sequence identity with the SMB domain of vitronectin, and 56% with that of ENPP1, displaying in both cases an rmsd of about 1.3 Å over 40 superposed Cαs; (**b**) The ATX and XaNPP phosphodiesterase (PDB:2GSN24) domains shown in matched orientations; the short loop (residues 274–280) that is more extended in *Xa*NPP (residues 154–178) is shown thicker and in ruby and the bound zinc ions are shown as grey spheres; the sequence identity between the two is 32%, with 1.5 Å rmsd over 335 superposed Cαs; (**c**) Side by side comparison of the ATX nuclease domain with the *A.sp* nuclease (PDB:1ZM830); the sequence identity is 19%, with 2.1 Å rmsd over 335 superposed Cαs. The EF-hand-like calcium (brown sphere) binding motif is at the bottom left and is absent in the bacterial nuclease; the *A.sp* ion binding sites are indicated with magenta spheres and are absent in the ATX domain.
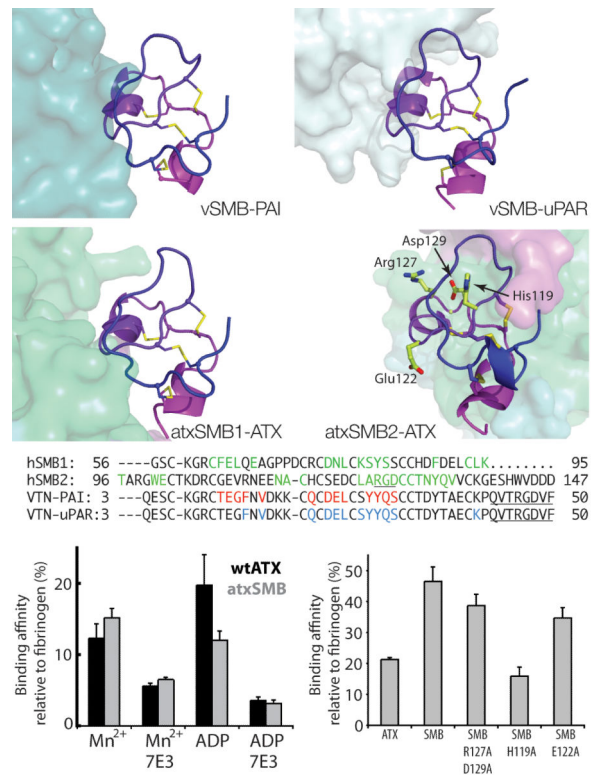
Figure 3.
The ATX catalytic site and substrate binding pocket. (**a**) The active site of ATX and (**b**) of *Xa*NPP (PDB: 2GSO24). Side chains atoms are shown as sticks, with the C_a atoms as spheres; all oxygen and nitrogen atoms are in red and blue respectively; Zn^{+2} ions are grey spheres; phosphate atoms are coloured orange; and vanadium atoms magenta; (**c**) A surface representation of the ATX binding site with the HA155 inhibitor buried in the binding pocket and shown as sticks with carbon atoms colored grey and the covalently bound boron pink; the ATX surface is green with the short loop that is more extended in *Xa*NPP and ENPP1 (residues 274–280) colored ruby; (**d**) The surface of *Xa*NPP coloured in aquamarine, superposed on the ATX complex with HA155; the extended *Xa*NPP- and ENPP1-specific loop (residues 154–178) in ruby, highlighting the absence of the hydrophobic pocket in *Xa*NPP; (**e**) The ATX substrate binding site shown as in (c) but with AMP superposed from the *Xa*NPP complex structure; (**f**) The *Xa*NPP surface with bound AMP (PDB: 2GSU24) shown as sticks; (**g**) The ATX surface colored by electrostatic potential (−70 to- 70 kT) to highlight the hydrophobic nature of the binding pocket, is shown together with a stick model of a docked LPC molecule; (**h**) A view similar to (g) colored as in (c),(e) and with the second SMB domain in magenta, highlighting the close interaction of the SMB domain with the lipid binding groove. The narrow tunnel is visible as a white hole in the middle.

Figure 4.
Biochemical analysis of human ATX and mutants. (**a**) A simplified drawing of the ATX binding pocket. The residues used for mutagenesis studies are indicated; (**b**) Modulation of LPC and pNP-TMP hydrolysis activity by ATX mutants, indicating the importance of specific residues for selectivity in LPC and nucleotide hydrolysis; (**c**) The A218V mutants prefers shorter chain lengths; the activity for WT *h*ATX and A218V mutant was normalized to 100% for LPC(14:0); (**d**) LPA(18:1) inhibition of nucleotide hydrolysis for wild-type ATX and SMB-ATX. All error bars represent the s.e.m.

Figure 5.
The SMB domains and integrin-mediated interaction with activated platelets. (**a**) The structure of the vitronectin SMB domain (vSMB) with plasminogen activator inhibitor 1 (PAI-1, PDB:1OC037). The SMB domain is shown as a cartoon, colored from purple through blue from the N- to the C-terminus, and the Cys-bridges are shown as yellow sticks. PAI-1 is shown as a surface colored aquamarine. The vSMB interaction surface with PAI-1 is 656 Å^2, making five hydrogen bonds and five salt bridges; (**b**) vSMB in complex with the urokinase-type plasminogen activator receptor (uPAR complex, PDB:3BT138) in light cyan. The vSMB interaction surface with uPAR is 620 Å^2, making seven hydrogen bonds and five salt bridges; (**c**) The first SMB domain of ATX (atxSMB1) highlighting the interaction with the rest of ATX, shown as a surface colored as in Fig.1. The atxSMB1 interaction surface with the PDE is 620 Å^2, making nine hydrogen bonds and a salt bridge; (**d**) The second SMB domain (atxSMB2) with the rest of ATX. The atxSMB2 interaction surface with the PDE is 571 Å^2, but forming only three hydrogen bonds; (**e**) An alignment of vitronectin and ATX SMB sequences; residues involved in interaction with binding partners are in color; the RGD motifs are underlined; (**f**) Binding of wild-type ATX and atxSMB to activated platelets is similar in magnitude, depends on Mn^{+2} and ADP, and can be lowered by interference with an integrin β3 binding antibody. (**g**) Binding of the atxSMB domains to platelets is significantly attenuated by mutation of His-119 to alanine and less affected by mutation of the RDB motif. All error bars represent the s.e.m.

Table 1

Data collection and refinement statistics

	Native + I	Native 2	HA155 Inhibitor
Data collection			
Space group	P1	P2$_1$2$_1$2$_1$	P2$_1$2$_1$2$_1$
Cell dimensions			
a, b, c(Å)	53.8, 63.3, 70.5	95.3, 121.8, 158.4	63.99, 90.2,152.7
α, β, γ(°)	98.8, 106.2, 99.8	90.0, 90.0, 90.0	90.0, 90.0, 90.0
Resolution (Å)	20.0–2.05 (2.12–2.05)	20.0–2.6 (2.74–2.6)	20.0–3.2 (3.36–3.2)
R_{merge}	0.097 (0.378)	0.191 (0.488)	0.128 (0.571)
I / σI	13.9 (2.5)	7.7 (1.5)	10.3 (3.5)
Completeness (%)	96.8 (93.9)	91.9 (69.7)	98.5 (98.5)
Redundancy	4.8(3.0)	3.1 (1.8)	6.0 (5.6)
Refinement			
Resolution (Å)	20.0–2.05	20.0–2.6	20.0–3.2
No. reflections	49561	49273	15034
R_{work} / R_{free}	17.2 / 22.0	21.6 / 27.5	20.1 / 25.5
No. atoms			
Protein	6396	12333	6140
Ligand/Ion/Glycan	5/3/39	-/6/56	34/3/39
Water/Iodine	332/28	19/-	11/6
B-factors			
Protein	38	29	53
Ligand/ion/Glycan	34/35/42	-/30/27	40/40/56
Water/Iodine	24/51	6/-	23/9
R.m.s. deviations			
Bond lengths (Å)	0.017	0.013	0.008
Bond angles (°)	1.62	1.52	0.93

For the 'Native + I' and 'HA155 Inhibitor' datasets a single crystal was sued. For the 'Native 2' dataset two crystals were used.